EFFECT OF THE CALCINATION TEMPERATURE ON THE PROPERTIES OF MnOx–CuO–ZrO2–CeO2 CATALYSTS FOR CO OXIDATION

O. A. Bulavchenko[1]*, T. N. Afonasenko[2],
V. P. Konovalova[1], V. A. Rogov[1],
E. Yu. Gerasimov[1], E. E. Aidakov[1,3],
and Z. S. Vinokurov[1,3]

Four-component oxide catalysts MnO_x–CuO–ZrO_2–CeO_2 are synthesized by co-precipitation with varying the calcination temperature from 400 °C to 800 °C. Formation and decomposition processes in mixed oxides are studied by X-ray diffraction, transmission electron microscopy, and X-ray photoelectron spectroscopy. The *redox* properties of the obtained samples are tested by temperature-programmed hydrogen reduction, and the catalytic characteristics are examined in the CO oxidation reaction. At 400-600 °C homogeneous solid solution $Mn_xCu_yZr_zCe_qO_2$ with the fluorite structure is formed. Temperature elevation to 700-800 °C facilitates the gradual decomposition of initial oxide, with manganese and copper cations leaving its composition in the form of highly dispersed CuO and $Cu_xMn_{3-x}O_4$ particles. The occurrence of different active states in the catalyst and their transitions into each other under the temperature effect is shown to maintain the high activity in the CO oxidation reaction up to 800 °C.

INTRODUCTION

A steady growth in fuel production and consumption increases the amount of pollutants in the atmosphere. The main sources of pollutants are motor transport, thermal power stations, and fabric, solvent, and dye industries. Among diverse technologies intended to decrease exhausts, catalytic oxidation is most appropriate to remove a considerable amount of volatile organic compounds (VOCs) and CO, NO_x owing to its high efficiency and low energy costs. Catalytic technologies are promising for gas purification. They make it possible to process multicomponent gases with low initial concentrations of hazardous substances, to achieve high degrees of purification, to conduct the continuous process, and in most cases, to avoid the formation of secondary pollutants. At present, the proposed afterburner catalysts contain, as a rule, precious metals or complex oxides. Oxides of transition and rare earth metals is an alternative to precious metals in catalytic complete oxidation processes. Despite that these systems are relatively less active, their undisputable advantages are low cost, thermal resistance,

[1]Boreskov Institute of Catalysis, Siberian Branch, Russian Academy of Sciences, Novosibirsk, Russia; *obulavchenko@catalysis.ru. [2]Center of New Chemical Technologies, Institute of Catalysis, Siberian Branch, Russian Academy of Sciences, Omsk, Russia. [3]Synchrotron Radiation Facility "SKIF", Boreskov Institute of Catalysis, Siberian Branch, Russian Academy of Sciences, Koltsovo, Russia. Original article submitted February 9, 2024; revised March 14, 2024; accepted March 15, 2024.

long service life, regeneration ability, and availability of a large number of simple and mixed oxides [1-4]. Therefore, the search for new environmentally friendly and cheap complete-oxidation-catalysts, including multicomponent systems, is urgent.

Ceria together with other metals are now widely used in the composition of complete- oxidation-catalysts [5, 6]. It is applied in the composition of automotive catalysts, and its role is to increase the oxygen capacity of a system. These properties of the oxide are due to the cerium cation ability to rapidly change the charge state ($Ce^{3+} \rightarrow Ce^{4+}$), which allows it to easily store and release oxygen. The addition of a dopant to cerium oxide significantly changes its characteristics. Thus, when cerium is substituted by cations with an oxidation state less than four, the number of structural defects and oxygen capacity can increase in CeO_2 (anion vacancies can form) [7, 8], which in turn is reflected on the catalytic properties in CO and hydrocarbon oxidation reactions.

The introduction of a heteroatom into the cerium oxide matrix causes various synergy phenomena resulting in the formation of not only solid solution but also a contact between segregated oxide and the deposition of nanoparticles on the surface [9]. Many recent works have been devoted to studies of Mn-doped CeO_2. It is shown that these systems are highly active in catalytic oxidation reactions of CO and VOC as well as soot [10-14]. Nanoparticles MnO_x with a high specific surface area and weakly bound oxygen can form in the interaction of oxides, which results in prominent catalytic properties in oxidation reactions. Moreover, the introduction of the second element usually influences the oxide dispersion and decreases the particle size. At the same time, in the interaction of manganese and ceria, solid solutions can form, which are characterized by the occurrence of oxygen vacancies. The latter improve oxygen adsorption from the gas phase and facilitate its migration to the oxide structure, owing to which considerable amounts of active surface oxygen are formed. However, the stability of MnO_x–CeO_2 catalysts is low. Thermal treatment at 500 °C deactivates the catalyst because the $Mn_xCe_{1-x}O_{2-\delta}$ solid solution decomposes and the specific surface area drastically decreases [11-13]. One of the ways to improve the thermal stability of MnO_x–CeO_2 catalysts is the introduction of additional components. For instance, zirconium produces a positive effect: it prevents the agglomeration and formation of large CeO_2 particles [15-19]. Triple systems MnO_x–ZrO_2–CeO_2 demonstrated thermal stability up to 650 °C without a significant loss of activity owing to the presence of zirconium in the catalyst composition [18]. Tin oxide is also used as a dopant to CeO_2-based complete-oxidation-catalysts because it affects the thermal stability and formation of oxygen vacancies [20-22]. The introduction of copper has a positive effect on the catalytic properties and stability. This is explained not only by the additional formation of defects but also the interaction of manganese and copper oxides. Mixed Mn–Cu oxides are known to have own catalytic activity in complete oxidation reactions, including CO selective oxidation reactions [23-26]. For instance, hopcalite based on manganese and copper mixed oxide is a well-known example of the CO oxidation catalyst that is widely used in the personal respiratory protection equipment [27, 28].

In this work, we considered quaternary systems MnO_x–CuO–ZrO_2–CeO_2 obtained by co-precipitation with variation of the calcination temperature. The genesis of the active component was investigated depending on the preparation conditions. It is shown that main processes of the catalyst preparation is the formation of the $Mn_xCu_yZr_zCe_qO_2$ solid solution and its decomposition with the appearance of new types of CuO and $CuMn_2O_4$ active states. Different active components in the catalyst composition, changes in their nature, mutual transformations, temperature-induced transitions from one state into another - all this provides the improvement of the thermal stability, which is important in the context of increasing the stability of ceria-based catalysts. The synthesized MnO_x–CuO–ZrO_2–CeO_2 catalysts were analyzed by a set of physicochemical methods (powder XRD, TPR, XPS, PDF, TEM). The activity of these systems was tested in the CO oxidation reaction. It is shown that the presence of a multicomponent system supports thermal stability up to 800 °C. In the temperature range from 400 °C to 800 °C, the catalytic properties almost do not change during CO oxidation.

EXPERIMENTAL

Preparation of catalysts. The samples were prepared by precipitation. To a joint solution of $ZrO(NO_3)_2$, $Ce(NO_3)_3$, $Cu(NO_3)_2$, and $Mn(NO_3)_2$ salts a NaOH solution was added dropwise with constant stirring to pH = 11. Precipitation was performed at 75-80 °C. When precipitation completed, the obtained suspension was stirred for 1 h without heating. Then the suspension was left at room temperature overnight without stirring. The obtained precipitate was filtered off, washed with water on a filter to pH = 6-7. The samples were dried at 120 °C for 2 h and then calcined in a muffle furnace at 400-800 °C for 4 h. The cation ratio corresponded to the $Cu_{0.1}Mn_{0.1}Zr_{0.1}Ce_{0.7}O_2$ composition. A series of catalysts was denoted Cu0.1Mn0.1Zr0.1Ce0.7_*T*, where *T* is the synthesis temperature. The samples were fractioned and the 0.4-0.8 mm fraction was used in catalytic tests.

X-ray diffraction (XRD). XRD patterns were measured on a STOE STADI MP (Germany) powder diffractometer with a linear Mython2 1K (Decstris, Switzerland) detector and monochromatic $MoK_{\alpha 1}$ radiation, $\lambda = 0.709$ Å. XRD patterns were recorded in the 2θ range from 2° to 50° with a step of 0.015°. Unit cell parameters and phase ratios were estimated by the Rietveld method. For the correct determination of unit cell parameters the internal standard α-Al_2O_3 was used. The crystallite surface area was calculated from the XRD data in the assumption of their spherical shape by the following formula:

$$S_{XRD} = \frac{6000}{\rho \cdot D_{XRD}},$$

where ρ is the theoretical density of the material (g/cm^3); D_{XRD} are average CSR sizes. To estimate the degree of crystallite agglomeration the agglomeration coefficient (ξ) was evaluated based on the ratio of S_{BET} and S_{XRD} values

$$\xi = 1 - \frac{S_{BET}}{S_{XRD}}.$$

Pair distribution function (PDF) analysis. The XRD pattern for the analysis of the local structure of the catalyst by atomic PDF was obtained on a laboratory STOE STADI MP diffractometer with MoK_{α} radiation ($\lambda = 0.7093$ Å) in the 2θ range from 1.5° to 126.9° with a step of 0.015° and the acquisition time of 200 s.

The relationship between the atomic pair distribution function $G(r)$ and X-ray coherent scattering was found using the Fourier transform

$$G(r) = \frac{2}{\pi} \int_0^\infty Q \cdot i(Q) \cdot \sin(Qr) \cdot dQ,$$

where $Q = (4\pi \cdot \sin\theta)/\lambda$ is the absolute value of the wave vector; λ is the radiation wavelength; $i(Q)$ is the interference part of the scattering intensity. Functions $G(r)$ were obtained by data processing with the PDFgetX2 program [29], after which functions $G(r)$ were modeled in the PDFgui program [30].

The specific surface area of the catalysts was determined by the Brunauer–Emmett–Teller (BET) method using nitrogen adsorption isotherms measured at the liquid nitrogen temperature. The studies were carried out on an automated ASAP 2400 (Micromeritics Instrument Corp., USA) system.

Low-temperature nitrogen porometry was applied to determine the main texture characteristics. Before the measurement of N_2 adsorption isotherms at 77 K the 100-150 mg samples were subjected to the two-step vacuum thermal training in the measuring cell: at 300 °C for 10 h (heating rate 1 °C/min). Then the samples were heated to 350 °C with the same rate and kept at this temperature for 3 h until the attainment of constant pressure below 70 mTorr in the cell. The measurements were performed on Quadrasorb evo (Quantachrome Instruments, USA). The following texture characteristics were calculated from the adsorption isotherms using the instrumental software: total pore volume (V_{tot}, cm^3/g) at nearly atmospheric pressure; micropore (V_{micro}, cm^3/g) and mesopore (V_{meso}, cm^3/g) volumes determined by NLDFT from the adsorption branch of the adsorption isotherm in the approximation of the cylindrical pore shape [31]; macropore volume

(V_{macro}, cm^3/g) determined by BJH [32]. The pore size distributions were constructed by BJH and NLDFT (from the adsorption branches).

TEM was applied to obtain detailed information about the catalyst morphology and microstructure. For the analysis we used a ThemisZ (Thermo Fisher Scientific) microscope with a line resolution of 0.7 Å. EDX microanalysis of the elemental composition of the samples was carried out using a SuperX Thermo Fisher Scientific spectrometer.

TPR in hydrogen was performed in a flow quartz reactor equipped with a thermal conductivity detector. The 10% H$_2$ feed rate to Ar was 40 mL/min, the heating rate from room temperature to 900 °C was 10 °C/min. The TPR curves were described by the Gaussian in the Fityk program. The mass center temperature was calculated by the following formula:

$$T_{mc} = \frac{\sum X_i \cdot Y_i}{\sum Y_i},$$

where X_i is the position of this point in the temperature axis; Y_i is the intensity at this point. Calculations were performed for the temperature range from 50 °C to 320 °C.

XPS. The chemical composition of the sample surface was analyzed on a SPECS Surface Nano Analysis GmbH (Germany) spectrometer. The spectrometer was equipped with a hemispherical PHOIBOS-150-MCD-9 analyzer, a FOCUS-500 X-ray monochromator, and an XR-50M source with a Al/Ag dual anode. The spectra were recorded with non-monochromatized AlK_α radiation ($h\nu$ = 1486.61 eV). The binding energy scale (E_b) was calibrated using the internal standard by the Ce3$d_{3/2}$-U‴ peak contained in the support composition (E_b = 916.7 eV). The relative concentration of elements in the analysis region was determined based on the integrated intensity of XPS lines with regard to the photoionization cross-sections of the respective terms [33]. For the detailed analysis the spectra were decomposed into individual components. After the Shirley background subtraction [34] the experimental curve was fitted by a series of peaks corresponding to electron photoemission from atoms in different chemical environments. The data were processed using the CasaXPS program package. The peak shape was approximated by the symmetric function obtained by summing Gaussians and Lorentzians.

Catalytic tests. The samples were tested in the CO oxidation reaction on a flow apparatus in a glass reator (170 mm × ⌀ 10 mm). The initial gas mixture had the composition: 1% CO and 99% air, total consumption 487 mL/min. The reaction mixture before and after the reactor was analyzed on a LKhM-8MD chromatograph with mixture separation on a packed column filled with CaA (3m) zeolite. The amount of unreacted CO was determined by the thermal conductivity detector. The catalyst sample of 0.3 g was mixed with quartz to a volume of 3 mL. The temperature in the catalyst layer was controlled and varied using a chromel alumel thermocouple connected with the VARTA thermoregulator. To calculate the degree of CO conversion (X_{CO}) we used the formula

$$X_{CO} = [(P_{CO} / P_{N_2})_{IN} - (P_{CO} / P_{N_2})_{OUT}] / (P_{CO} / P_{N_2})_{IN},$$

where P_{CO}, P_{N_2} are the areas of CO and nitrogen peaks before (IN) and after (OUT) the reaction (P_{N_2} area was used as the internal standard).

RESULTS AND DISCUSSION

Structural and microstructural properties of the catalysts. Fig. 1 depicts the XRD patterns of the Cu0.1Mn0.1Zr0.1Ce0.7 series of catalysts with varying the synthesis temperature and model curves of certain phases. The XRD patterns of catalysts obtained at 400-800 °C are similar: peaks are observed at 2θ = 13.1°, 15.1°, 21.4°, 25.2°, 30.5°, 33.3°, 34.2°, 37.6°, 39.9°, 43.6°, 45.7° and correspond to 111, 200, 220, 311, 400, 331, 420, 422, 333, 440, 531 reflections of CeO$_2$ with the fluorite structure (PDF No. 34-394). No XRD peaks corresponding to manganese- or copper-containing oxide phases were observed for catalysts obtained at 400-600 °C. With an increase in the calcination temperature to 700 °C additional peaks appear corresponding to CuO (PDF No 45-937) and Cu$_x$Mn$_{3-x}$O$_4$ mixed oxide based on the CuMn$_2$O$_4$ phase (PDF No. 35-1029) with the cubic spinel structure. It is also can be noted that the peaks of initial fluorite-type oxide are split.

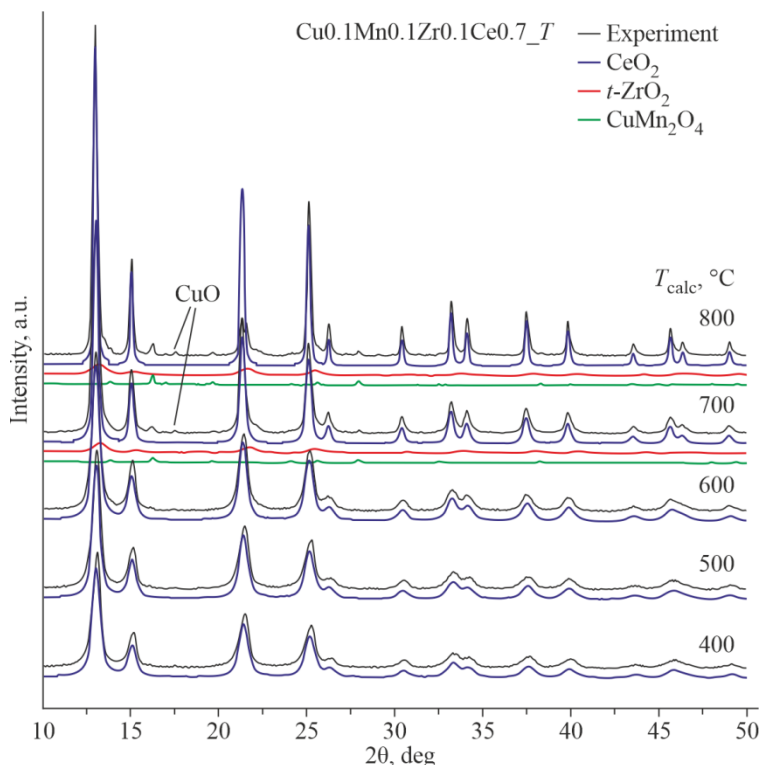**Fig. 1.** Powder XRD patterns of initial samples of the Cu0.1Mn0.1Zr0.1Ce0.7_*T* series where *T* is the calcination temperature and model curves of certain phases. Wavelength $\lambda = 0.709$ Å.

It is seen that on the right of 111 and 220 reflections ($2\theta = 13.1°$ and $21.4°$) an additional shoulder appears at $2\theta = 13.6°$, $21.9°$. This fact can indicate the formation of oxide of the tetragonal ZrO_2 type (PDF No. 50-1089). Structural characteristics of the catalysts, which were calculated by the Rietveld refinement, are listed in Table 1. For Cu0.1Mn0.1Zr0.1Ce0.7_400 the oxide unit cell parameter is 5.391(1) Å; this value is smaller than that of pure CeO_2 (5.411 Å, PDF No. 34-394). A change in the unit cell parameter testifies the formation of a $Ce(Mn,Cu,Zr)O_2$ solid solution. Since the ionic radii of zirconium and manganese cations are smaller than the cerium ionic radius (Mn^{2+} - 0.097 nm, Mn^{3+} - 0.065 nm, Mn^{4+} - 0.053 nm, Zr^{4+} - 0.084 nm, Cu^{2+} - 0.072 nm, Ce^{4+} - 0.097 nm [35]), the introduction of these elements results in the observed decrease in unit cell parameters. When the calcination temperature is elevated from 400 °C to 800 °C, the unit cell parameter increases from 5.391(1) Å to 5.404(1) Å, which is accompanied by the appearance of crystalline manganese, copper, and zirconium oxides. The initial solid solution seems to decompose into two phases based on ZrO_2 and CeO_2. Unit cell parameters of these phases also differ from the values corresponding to pure zirconia and ceria, therefore in this case, we can speak about the formation of two solid solutions with different compositions: *t*-$Zr(Mn,Cu,Ce)O_2$ based on tetragonal ZrO_2 and $Ce(Mn,Cu,Zr)O_2$ with the fluorite structure (Table 1). At the same time, Mn and Cu cations are released as different oxides. Estimates of the composition show that for catalysts calcined at 700-800 °C, 17-19 wt.% of mixed oxide based on tetragonal ZrO_2, 1-2 wt.% CuO, and 3-5 wt.% $Cu_xMn_{3-x}O_4$ are released, with average CSR sizes of the oxides formed being 40 Å for ZrO_2, 175-210 Å for CuO, and 150-180 Å for $Cu_xMn_{3-x}O_4$.

As the synthesis temperature is elevated from 400 °C to 800 °C, average sizes of CSR of the main phase (CeO_2-based mixed oxide) increase from 50 Å to 180 Å. The specific surface area decreases from 93 m^2/g to 7.4 m^2/g (Table 1) along with the pore volume (Table 1). The catalysts obtained at 400-600 °C have a mixed porous structure, and at 700-800 °C they become mesomacroporous. It should be noted that in the catalysts obtained at 400-600 °C, the specific surface area decreases almost two times (from 93 m^2/g to 45 m^2/g), however, the average CSR sizes increase insignificantly - from 50 Å

TABLE 1. Phase Composition, Unit Cell Parameters, Average CSR Sizes, Specific Surface Area (S_{BET}), Agglomeration Coefficient (ξ), Total Pore Volume (V_{tot}), Volumes of Micropores (V_{micro}), Mesopores (V_{meso}), and Macropores (V_{macro}) of Cu0.1Mn0.1Zr0.1Ce0.7 Catalysts Depending on the Synthesis Temperature (T_{calc})

T_{calc}, °C	Phase composition, wt.%	Unit cell parameter, Å	CSR, Å	S_{BET}, m²/g	ξ[#2]	V_{micro}, V_{meso}, V_{macro}, cm³/g	V_{tot}, cm³/g
400	CeO$_2$[#1]	5.391(1)	50(5)	93	0.50	0.004 0.105 0.046	0.13
500	CeO$_2$[#1]	5.397(1)	50(5)	58	0.69	0.002 0.095 0.036	0.125
600	CeO$_2$[#1]	5.398(1)	55(5)	45	0.74	0.001 0.091 0.045	0.12
700	79% CeO$_2$[#1] 17% t-ZrO$_2$[#1] 3% Cu$_x$Mn$_{3-x}$O$_4$ 1% CuO	5.404(1) 5.298(6)[#1] 8.318(3) –	100(10) 40(4) 150(15) 175(18)	19	0.80	0 0.074 0.077	0.14
800	74% CeO$_2$[#1] 19% t-ZrO$_2$[#1] 5% Cu$_x$Mn$_{3-x}$O$_4$ 2% CuO	5.404(1) 5.317(8)[#1] 8.310(2) –	180(18) 40(4) 180(18) 210(20)	7.4	0.86	0 0.045 0.040	0.078

[#1] CeO$_2$ solid solution Ce(Mn, Cu, Zr)O$_2$ based on cubic CeO$_2$; t-ZrO$_2$ based on ZrO$_2$ with the tetragonal (t) structure; unit cell parameter of t-ZrO$_2$ in the cubic approximation.

[#2] $\xi = 1 - \dfrac{S_{BET}}{S_{XRD}}$. In the approximation of the spherical particle shape $S_{XRD} = \dfrac{6000}{\rho \cdot D_{XRD}}$, where ρ is the theoretical density of the material (g/cm³); D_{XRD} are average CSR sizes.

to 55 Å. Therefore the agglomeration coefficient illustrating the relationship between the specific surface area and average CSR sizes was additionally calculated for these samples in the spheric particle approximation. At calcination temperatures of 400-600 °C the coefficient changes within 0.50-0.74, which corresponds to the behavior of Ce–Zr mixed oxides [36].

To identify possible dispersed states in multicomponent catalysts (Cu0.1Mn0.1Zr0.1Ce0.7_400 and Cu0.1Mn0.1Zr0.1Ce0.7_600) PDFs were applied. Fig. 2a, b depicts the experimental atomic pair distribution function $G(r)$ of the Cu0.1Mn0.1Zr0.1Ce0.7_400 sample. It is seen that all coordination peaks of this function correspond to distances characteristic of the fluorite structure.

Experimental function $G(r)$ is described by the model function of the Cu$_{0.1}$Mn$_{0.1}$Zr$_{0.1}$Ce$_{0.7}$O$_2$ solid solution with the cubic fluorite structure. The curves are inconsistent in peak intensities, and the inconsistency increases with distance due to the size effect. To correlate the peak intensities of the experimental and model functions the particle size was refined, and it was 45 Å (Fig. 2b). This value is consistent with the CSR size of mixed oxide (Table 1). Model function $G(r)$ well agrees with the experimental data ($R_w = 0.099$). It should be emphasized that no additional coordination peaks corresponding to other distances were observed in the PDF curve. Fig. 2c, d depicts experimental function $G(r)$ for the Cu0.1Mn0.1Zr0.1Ce0.7_600 catalyst. Model function $G(r)$ was also calculated based on the solid solution phase with the CeO$_2$ structure. According to the results of the refinement, the particle size was 50 Å for the Cu0.1Mn0.1Zr0.1Ce0.7_600 catalyst ($R_w = 0.098$). Additional coordination peaks were also not observed in experimental curve $G(r)$.
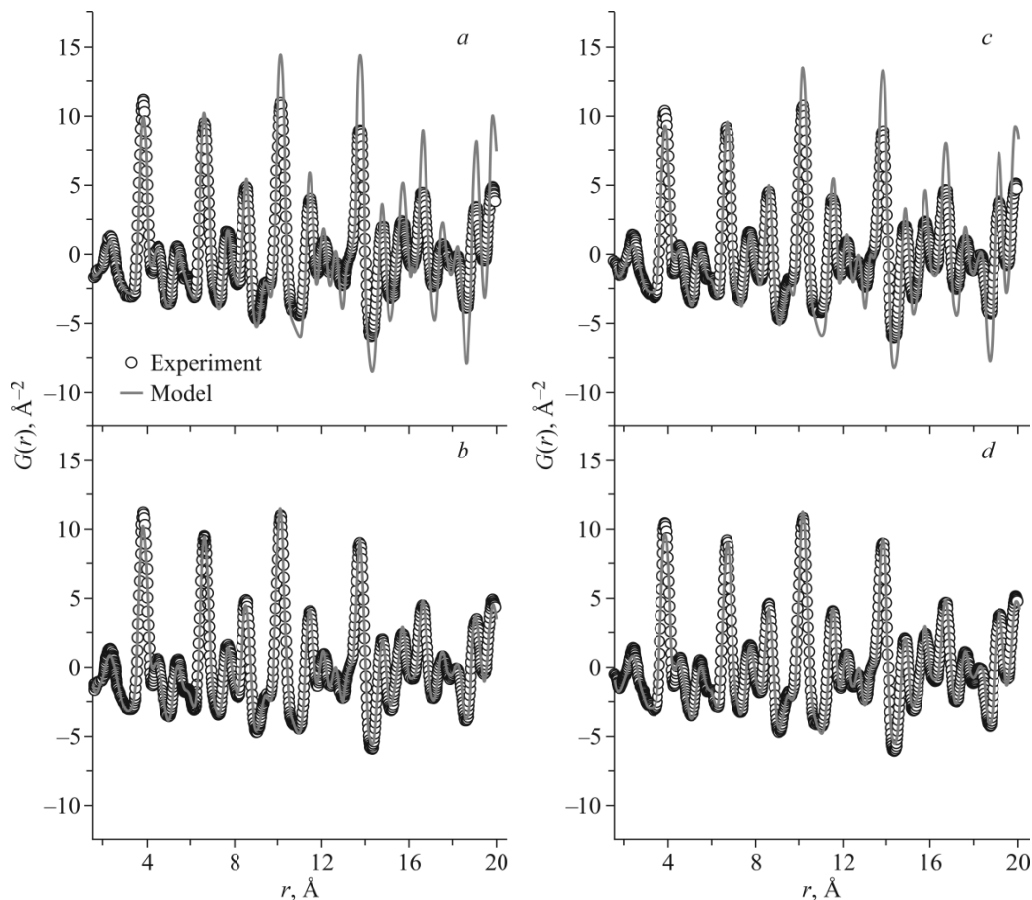
Fig. 2. Experimental and model functions $G(r)$ of the Cu0.1Mn0.1Zr0.1Ce0.7_400 catalyst without taking into account the particle size (*a*) and for 45 Å spherical particles (*b*); the Cu0.1Mn0.1Zr0.1Ce0.7_600 catalyst without taking into account the particle size (*c*) and for 50 Å spherical particles (*d*); the model represents a solid solution based on the CeO_2 structure (space group $Fm\overline{3}m$).

Thus, according to the PDF analysis data, both catalysts represent the $Ce(Mn,Cu,Zr)O_2$ solid solution with the fluorite structure. A change in the calcination temperature from 400 °C to 600 °C insignificantly affects the local structures of the catalysts.

Fig. 3 presents TEM images of the Cu0.1Mn0.1Zr0.1Ce0.7_600 sample. According to the TEM data, the catalyst consists of 5-10 nm round particles combined in large aggregates up to 500 nm (Fig. 3*a, b*). EDX mapping revealed the primarily uniform distribution of elements over the catalyst volume (Fig. 3*c, d*). Separate phases containing copper and/or manganese were not detected, which correlates with the powder XRD and PDF analysis data (Figs. 1, 2).

Thus, the powder XRD, PDF, and TEM results confirm the formation of the single-phase solid solution for the catalyst synthesized at 400 °C, with it being stable up to 600 °C.

Study of *redox* properties. The TPR-H_2 was applied to evaluate changes in the redox properties of Cu0.1Mn0.1Zr0.1Ce0.7 catalysts at calcination temperature variation. According to TPR-H_2 curves (Fig. 4) of a series Cu0.1Mn0.1Zr0.1Ce0.7, there is a wide halo at reduction temperatures of 700-900 °C. It is characteristic of CeO_2-based samples and is due to partial reduction of cerium from 4+ oxidation state to 3+ [37].

The low-temperature range of 100-300 °C (Fig. 4*a*) contains poorly resolved peaks with maxima at 141-166 °C, 175-199 °C, 195-241 °C. According to the literature data, the mentioned peaks are associated with both reduction of highly dispersed CuO particles and mixed oxide $Cu_xMn_{3-x}O_4$ [26, 27, 38-40]. According to the powder XRD and TEM studies (Figs. 1, 3), the presence of the $Ce(Mn,Cu,Zr)O_2$ solid solution is observed in the Cu0.1Mn0.1Zr0.1Ce0.7 catalysts up to the
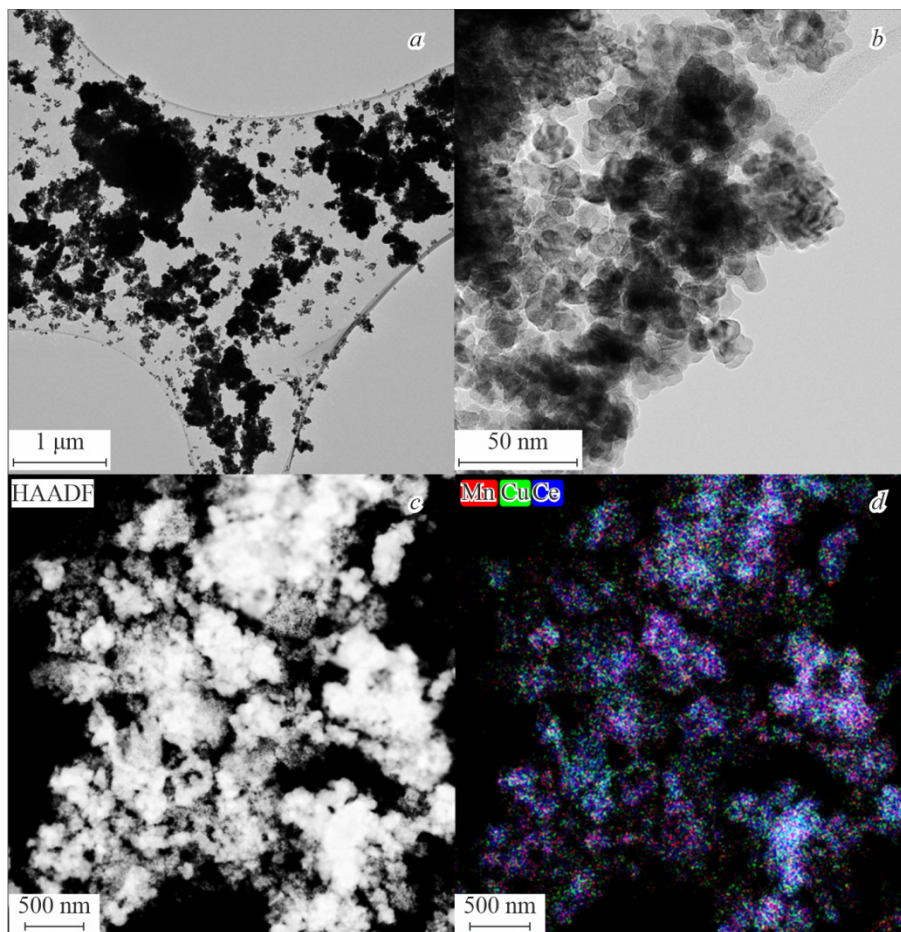
Fig. 3. TEM images (*a*, *b*), dark-field image (*c*), EDX mapping (*d*) of Cu0.1Mn0.1 Zr0.1Ce0.7_600 where Mn is shown by red, Cu - green, Ce - blue (see el. version).
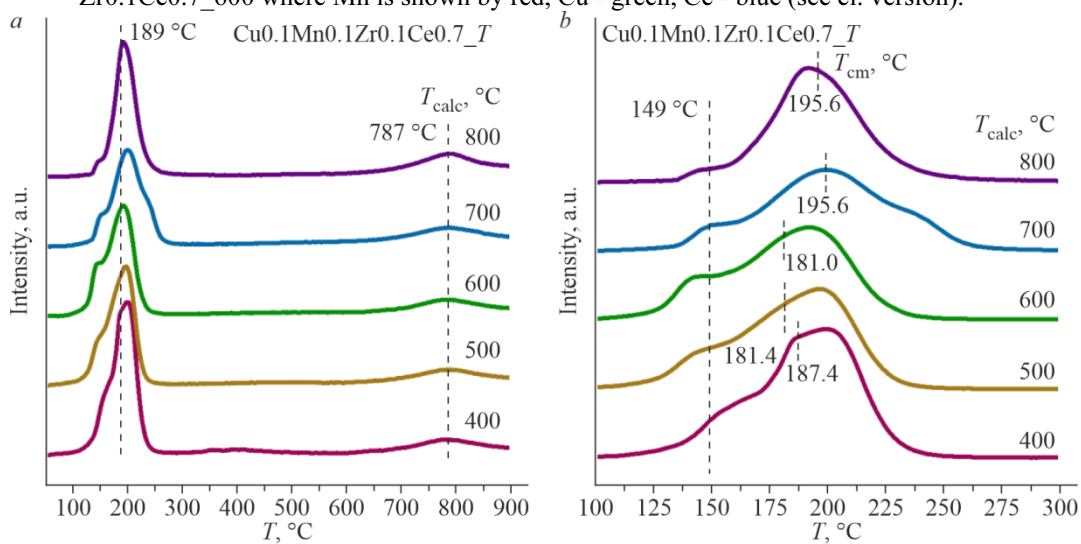
Fig. 4. TPR-H_2 curves of samples of the Cu0.1Mn0.1Zr0.1Ce0.7_*T* series where *T* is the calcination temperature. General form of TPR-H_2 curves (*a*), blue lines depict average T_{MC} peaks of low- and high-temperature ranges. TPR-H_2 curves of the low-temperature range from 100 °C to 300 °C (*b*); colored lines denote T_{MC} of peaks of the respective samples; black line is drawn to visualize a change in the temperature of the first peak.

synthesis temperature of 600 °C, which is consistent with the TPR data. In Fig. 4b it is seen that in the calcination temperature range of 400-600 °C, the TPR curves are similar, but there is a shift of peaks to lower temperatures (Table 2). This behavior reflects the evolution of the weakly bound oxygen state in the composition of the solid solution, i.e., elevation of the calcination temperature destabilizes the structure of the solid solution. A further increase in the calcination temperature leads to the decomposition of the solid solution, and correspondingly, a strong change in the form of TPR curves. A general redistribution of TPR peak intensities to higher temperatures is also observed, which we relate to the contribution of new phases of CuO and $Cu_xMn_{3-x}O_4$ oxides.

Analysis of the charge states of elements and surface ratios. To evaluate changes in the electronic properties and element ratios on the surfaces of Cu0.1Mn0.1Zr0.1Ce0.7 catalysts we used XPS. Atomic ratios of elements in the near-surface layer of the samples, which were found from the XPS data, are listed in Table 3. The Zr 3d, Ce 3d, Cu 2p, and Mn 2p spectra are shown in Fig. 5.

The Zr 3d spectra are well described by one Zr $3d_{5/2}$–Zr $3d_{3/2}$ doublet with the Zr $3d_{5/2}$ binding energy of 181.9 eV (Fig. 5a). The Zr $3d_{5/2}$ binding energy is characteristic of the Zr^{4+} state. For instance, for stoichiometric ZrO_2 the $Zr3d_{5/2}$ binding energies are within 181.9-182.3 eV [41]. Cerium is in the Ce^{3+} and Ce^{4+} states. The Ce3d spectra are known to have a complex shape (Fig. 5b). Firstly, as a result of the spin-orbit interaction, the Ce 3d level is split into two sublevels Ce $3d_{5/2}$ and Ce $3d_{3/2}$, which leads to the appearance of a doublet in the XPS spectrum. The ratio of its integrated line intensities is 3:2. Secondly, each component of the doublet is in turn split into three peaks for CeO_2 (v/u, v″/u‴, v‴/u‴) or two peaks for Ce_2O_3 (v′/u′, v_0/u_0). Having determined the relative intensities of these components, it is possible to estimate the fraction of Ce^{4+} ions [41]. In accordance with results of fitting the spectra by individual components, the fraction of Ce^{3+} ions is in the range of 10-15% for all samples (Table 3).

Fig. 5c depicts the Mn 2p spectra of the samples studied. To identify the manganese states the binding energy of the Mn $2p_{3/2}$ peak was used together with the presence and positions of shake-up satellites [42]. For manganese in MnO, Mn_2O_3, and MnO_2 compositions the literature gives Mn $2p_{3/2}$ binding energies in the ranges of 640.4-641.7 eV, 641.5-641.9 eV, and 642.2-642.6 eV respectively [41, 42]. The difference in binding energies of different manganese states can be less than 0.2 eV (e.g., for MnO_2 and Mn_2O_3). The analysis of the Mn 2p spectrum is hindered for this series because of the low signal intensity. The quntitative determination of different manganese states by fitting with components is highly erroneous. The

TABLE 2. TPR Data for Cu0.1Mn0.1Zr0.1Ce0.7 Samples Depending on the Calcination Temperature: T_{CM} in the Low-Temperature Range (up to 300 °C) and Total Hydrogen Absorption (up to 900 °C)

Synthesis temperature, °C	Low-temperature range T_{CM}, °C	Total hydrogen absorption, mmol H_2/g
400	187.4	0.235
500	181.4	0.204
600	181.0	0.197
700	199.0	0.201
800	195.6	0.193

TABLE 3. Atomic Ratios of Elements in the Near-Surface Layer of Cu0.1Mn0.1Zr0.1Ce0.7_T Catalysts Depending on the Calcination Temperature (T)

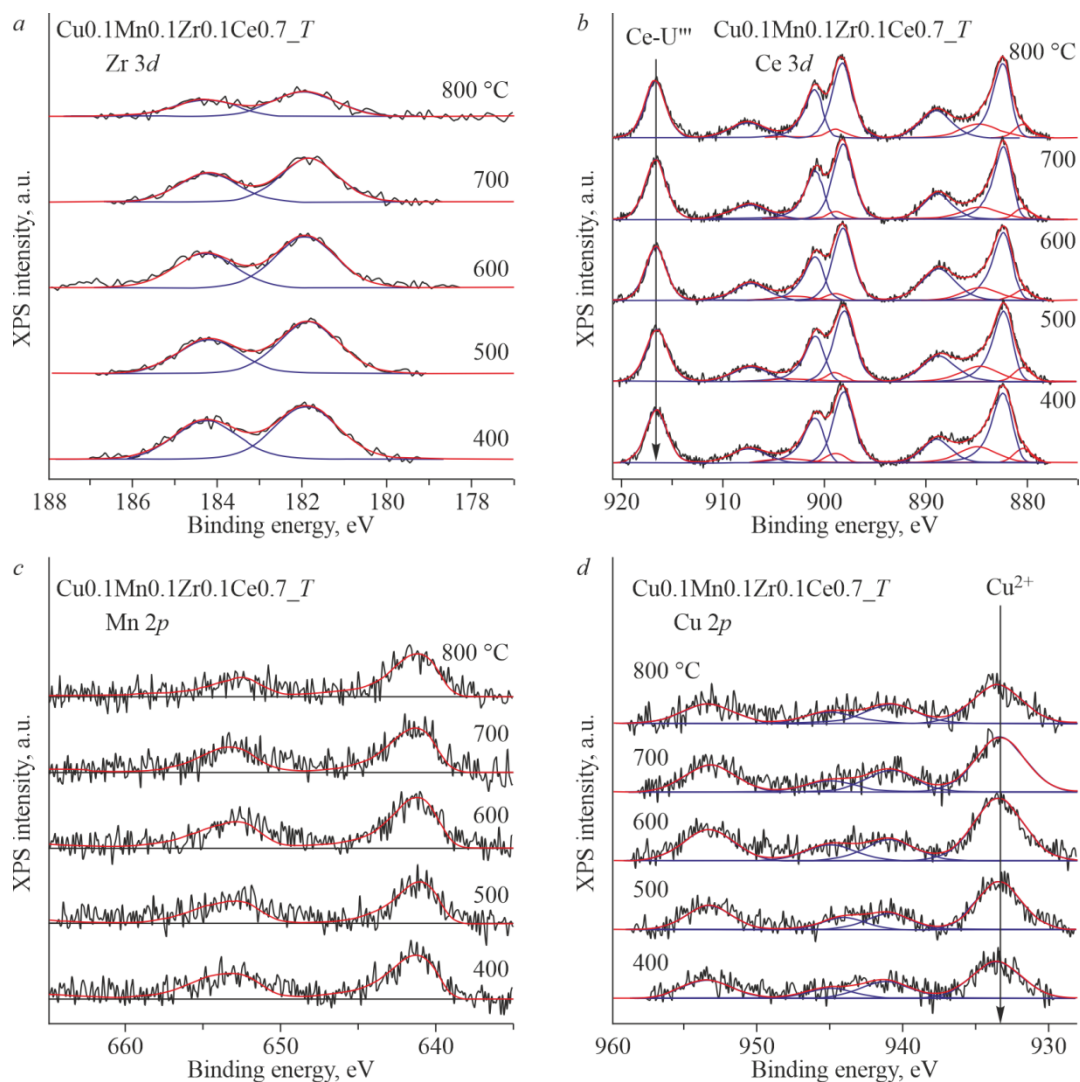| Synthesis temperature, °C	[Mn]/[Ce]	[Cu]/[Ce]	[Zr]/[Ce]	Ce^{3+}, %
400	0.28	0.32	0.40	14
500	0.30	0.40	0.35	14
600	0.29	0.46	0.35	11
700	0.33	0.41	0.26	10
800	0.20	0.38	0.14	13

Fig. 5. Zr 3*d* (*a*), Ce 3*d* (*b*), Mn 2*p* (*c*), Cu2*p* (*d*) spectra of the studied samples of the Cu0.1Mn0.1Zr0.1Ce0.7_*T* series where *T* is the calcination temperature. The spectra are normalized to the integrated intensity of the Ce 3*d* spectrum.

Mn 3*s* multiplet splitting value, which allows the clarification of Mn oxidation states, is also analyzed. The literature reports the multiplet splitting values of 5.7-6.2 eV for Mn(II) oxides, 4.6-5.4 eV for Mn(III) (4.6 eV for MnOOH, selected values for Mn_2O_3 are 5.2-5.4 eV), and 4.5-4.7 eV for Mn(IV) [43-45] The multiplet splitting value is in the range of 5.5-5.7 eV for all samples, which can correspond to several manganese oxides. The use of Mn 3*s* multiplet splitting values do not enable the unambiguous determination of the manganese oxidation state for this series of catalysts. Therefore, we decided not to fit the Mn 2*p* spectrum with components and give only the quantitaive estimate of the total manganese amount in the sample (Table 3).

Fig. 5*d* presents the Cu 2*p* spectra of the studied samples. The shape of the Cu 2*p* spectrum indicates that copper is oxidized. The Cu 2*p* spectra demonstrate the Cu $2p_{3/2}$–Cu $2p_{1/2}$ doublet, the integrated line intensities of which have a 2:1 ratio, and two broad shake-up satellites. Their presence is characteristic of the Cu^{2+} state due to hybridization of Cu 3*d* and O 2*p* orbitals [46-48], and the integrated intensity of the shake-up satellite can reach 50% of the integrated intensity of the Cu $2p_{3/2}$ main peak [47, 49]. Shake-up satellites are absent in the spectra of Cu^{1+} and Cu^0. The Cu 2*p* spectra are similar for all samples and correspond to copper in the Cu^{2+} ground state.

Catalytic tests in the CO oxidation reaction. CO conversion curves *vs*. the process temperature are shown in Fig. 6*a* for the Cu0.1Mn0.1Zr0.1Ce0.7 samples. As seen, variation of the calcination temperature does not cause substantial shifts in the position of CO conversion curves relative to the reaction temperature. If the calcination temperature is increased from 400 °C to 500 °C, the CO conversion curve shifts to the low-temperature region and the temperature of 50% CO conversion (T_{50}) changes from 128 °C to 115 °C. At a further increase in the calcination temperature up to 700 °C no significant changes in the catalytic properties are observed. The CO conversion curves of the samples annealed at 500-700 °C are very similar, and T_{50} values are 113-115 °C. Only after the calcination of Cu0.1Mn0.1Zr0.1Ce0.7 at 800 °C the CO conversion curve only slightly shifts to high temperatures and the T_{50} value increases to 121 °C. For comparison we tested the Cu0.1Mn0.1Ce0.8 catalyst not containing Zr and calcined at 800 °C. The catalytic properties of this sample are much worse because its 50% CO conversion is reached at 203 °C. The observed superiority of Cu0.1Mn0.1Zr0.1Ce0.8 over Cu0.1Mn0.1Ce0.8 in the catalytic activity indicates the occurrence of the synergetic effect from the combined presence of cerium and zirconium in the CuO–MnO$_x$–ZrO$_2$–CeO$_2$ catalyst.

According to powder XRD, PDF, and TEM results, at synthesis temperatures above 400-600 °C the single-phase Mn$_x$Cu$_y$Zr$_z$Ce$_q$O$_2$ solid solution is formed, however, the temperature elevation only insignificantly increases average CSR sizes from 50 Å to 55 Å and decreases the specific surface area almost two times from 93 m^2/g to 45 m^2/g. It should be noted that changes in the CSR sizes are not that significant compared to the specific surface area, which is likely to be caused by rearrangements of the microstructure and changes in the agglomeration coefficient (Table 1). During a further increase in the synthesis temperature the Mn$_x$Cu$_y$Zr$_z$Ce$_q$O$_2$ solid solution decomposes, which is indicated by the appearance of CuO and Cu$_x$Mn$_{3-x}$O$_4$, *t*-Zr(Mn,Cu,Ce)O$_2$ reflections in the XRD patterns of oxides. This process is accompanied by a further decrease in the specific surface area, however, the activity remains stable, which can be indicative of a change in the nature of active phases. Thus, at low temperatures mainly the solid solution governed the catalytic properties because it is considered that when dopants are introduced into ceria, the oxygen mobility enhances due to the formation of oxygen vacancies [50].

In the temperature range of 400-600 °C no significant changes in the catalyst properties are observed, the phase and surface compositions and the local environment are stable. However, despite these facts, T_{50} lowers from 128 °C to 115 °C. Local heterogeneities are possible. The onset of the rearrangement is indicated by a small redistribution of hydrogen absorption peaks in the low-temperature range after the synthesis temperature of 600 °C (Table 2). At 700-800 °C the nature of dominant active centers changes, manganese and copper cations leaves the solid solution, and new phases appear. The detected change in the nature of active states seems to be the reason for stable catalytic properties in a wide range of synthesis
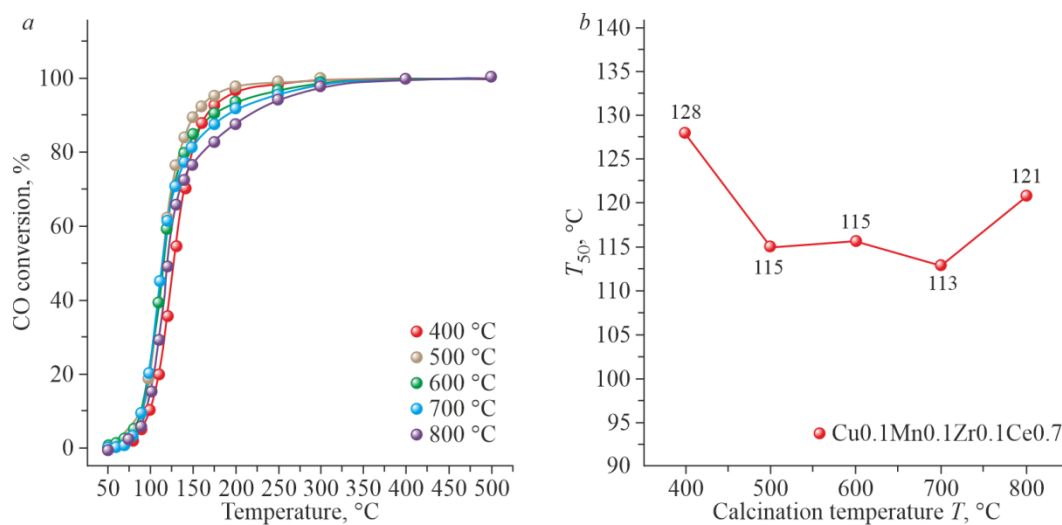

Fig. 6. Dependence of the degree of CO conversion on the reaction temperature for the catalyst: Cu0.1Mn0.1Zr0.1Ce0.7_T (*a*), 50% CO conversion temperatures (T_{50}) (*b*).

temperatures and indicates that the catalysts are thermally stable. The comparison with the Cu0.1Mn0.1Ce0.8 catalyst reveals that the addition of Zr to the catalyst appreciably enhances the catalyst stability; T_{50} for the samples calcined at 800 °C is 121 °C and 203 °C for the Cu0.1Mn0.1Zr0.1Ce0.7 and Cu0.1Mn0.1Ce0.8 catalysts respectively. We have previously observed the similar situation for the triple MnO_x–CeO_2–ZrO_2 system [18, 51]. A high catalytic activity in the CO oxidation reaction was observed in a wide range of the synthesis temperature of 500-700 °C (compared to 400-500 °C for MnO_x–CeO_2 catalysts), which is due to the occurrence of several types of centers and the presence of manganese both in the solid solution structure and as highly dispersed MnO_x particles on its surface and the transition from one state into another caused by the temperature effect. The addition of zirconium stabilized the fluorite structure and shifted the solid solution decomposition to the high-temperature range. The observed effect enhances for quaternary Cu0.1Mn0.1Zr0.1Ce0.7 systems and the range of constant catalytic characteristics substantially expands. On the one hand, this is explained by stabilization of the solid solution structure in a wide temperature range, and on the other hand, the formation of new active centers such as CuO and $Cu_xMn_{3-x}O_4$.

It is worth noting that the formation and decomposition of solid solutions with the fluorite structure as a way to obtain active states is often used in the synthesis of Ce- and Zr-containing catalysts. These processes are largely interconnected, and even a minor change in the temperature range of thermal treatment can result in releasing simple oxides or metal nanoparticles from the initial joint compound instead of the formation of homogeneous oxide. In some situations, this means that an unsuccessful synthesis yielding a catalyst inactive in the target reaction because of insufficient mixing of elements, the absence of a joint compound, and so on. In other situations, when the solid solution is partially or completely decomposed, nanoheterogeneous states can form which exhibit a high catalytic activity [52].

CONCLUSIONS

The effect of calcination temperature in the range from 400 °C to 800 °C is considered for a series of Cu0.1Mn0.1Zr0.1Ce0.7 catalysts obtained by co-precipitation. By powder XRD and TEM analyses it is shown that at 400 °C homogeneous solid solution $Mn_xCu_yZr_zCe_qO_2$ with the fluorite structure is formed. The temperature elevation to 700-800 °C causes the gradual decomposition of initial oxide with releasing manganese and copper cations in the form of highly dispersed CuO and $Cu_xMn_{3-x}O_4$ particles and decomposition of the initial state of the solid solution into oxides based on ZrO_2 and CeO_2. For the Cu0.1Mn0.1Zr0.1Ce0.7 series the catalytic activity almost does not change in the wide temperature range from 400 °C to 800 °C despite a significant decrease in the specific surface area. It is found that depending on the synthesis temperature, different types of active states are formed: solid solution $Mn_xCu_yZr_zCe_qO_2$, highly dispersed oxides CuO and $Cu_xMn_{3-x}O_4$. When the synthesis temperature is elevated, the decrease in the specific surface area is compensated by the appearance of more active states or an increase in their amount due to additional dispersion of the active component that occurs when the initial solid solution decomposes.

ACKNOWLEDGMENTS

FUNDING

CONFLICT OF INTERESTS

The authors of this work declare that they have no conflicts of interest.

REFERENCES

1. M. S. Kamal, S. A. Razzak, and M. M. Hossain. Catalytic oxidation of volatile organic compounds (VOCs) - A review. *Atmos. Environ.*, **2016**, *140*, 117-134. https://doi.org/10.1016/j.atmosenv.2016.05.031

2. R. J. Farrauto, M. C. Hobson, T. Kennelly, and E. M. Waterman. Catalytic chemistry of supported palladium for combustion of methane. *Appl. Catal.*, *A*, **1992**, *81*(2), 227-237. https://doi.org/10.1016/0926-860x(92)80095-t

3. S. Royer, and D. Duprez. Catalytic oxidation of carbon monoxide over transition metal oxides. *ChemCatChem*, **2011**, *3*(1), 24-65. https://doi.org/10.1002/cctc.201000378

4. H. Xu, N. Yan, Z. Qu, W. Liu, J. Mei, W. Huang, and S. Zhao. Gaseous heterogeneous catalytic reactions over Mn-based oxides for environmental applications: A critical review. *Environ. Sci. Technol.*, **2017**, *51*(16), 8879-8892. https://doi.org/10.1021/acs.est.6b06079

5. T. Montini, M. Melchionna, M. Monai, and P. Fornasiero. Fundamentals and catalytic applications of CeO_2-based materials. *Chem. Rev.*, **2016**, *116*(10), 5987-6041. https://doi.org/10.1021/acs.chemrev.5b00603

6. C. Sun, H. Li, and L. Chen. Nanostructured ceria-based materials: Synthesis, properties, and applications. *Energy Environ. Sci.*, **2012**, *5*(9), 8475. https://doi.org/10.1039/c2ee22310d

7. T. Andana, M. Piumetti, S. Bensaid, N. Russo, D. Fino, and R. Pirone. Nanostructured ceria-praseodymia catalysts for diesel soot combustion. *Appl. Catal.*, *B*, **2016**, *197*, 125-137. https://doi.org/10.1016/j.apcatb.2015.12.030

8. M. Nolan, S. C. Parker, and G. W. Watson. The electronic structure of oxygen vacancy defects at the low index surfaces of ceria. *Surf. Sci.*, **2005**, *595*(1-3), 223-232. https://doi.org/10.1016/j.susc.2005.08.015

9. E. W. McFarland and H. Metiu. Catalysis by doped oxides. *Chem. Rev.*, **2013**, *113*(6), 4391-4427. https://doi.org/10.1021/cr300418s

10. J. Du, Z. Qu, C. Dong, L. Song, Y. Qin, and N. Huang. Low-temperature abatement of toluene over Mn–Ce oxides catalysts synthesized by a modified hydrothermal approach. *Appl. Surf. Sci.*, **2018**, *433*, 1025-1035. https://doi.org/10.1016/j.apsusc.2017.10.116

11. X. Wu, S. Liu, D. Weng, F. Lin, and R. Ran. $MnO–CeO_2–Al_2O_3$ mixed oxides for soot oxidation: Activity and thermal stability. *J. Hazard. Mater.*, **2011**, *187*(1-3), 283-290. https://doi.org/10.1016/j.jhazmat.2011.01.010

12. X. Tang, Y. Li, X. Huang, Y. Xu, H. Zhu, J. Wang, and W. Shen. $MnO_x–CeO_2$ mixed oxide catalysts for complete oxidation of formaldehyde: Effect of preparation method and calcination temperature. *Appl. Catal.*, *B*, **2006**, *62*(3/4), 265-273. https://doi.org/10.1016/j.apcatb.2005.08.004

13. H. Zhang, J. Wang, Y. Cao, Y. Wang, M. Gong, and Y. Chen. Effect of Y on improving the thermal stability of $MnO_x–CeO_2$ catalysts for diesel soot oxidation. *Chin. J. Catal.*, **2015**, *36*(8), 1333-1341. https://doi.org/10.1016/s1872-2067(15)60867-1

14. M. V. Grabchenko, N. N. Mikheeva, G. V. Mamontov, V. Cortés Corberán, K. A. Litvintseva, V. A. Svetlichnyi, O. V. Vodyankina, and M. A. Salaev. Unraveling the structural and compositional peculiarities in CTAB-templated $CeO_2–ZrO_2–MnO_x$ catalysts for soot and CO oxidation. *Nanomaterials*, **2023**, *13*(24), 3108. https://doi.org/10.3390/nano13243108

15. T. Rao, M. Shen, L. Jia, J. Hao, and J. Wang. Oxidation of ethanol over Mn–Ce–O and Mn–Ce–Zr–O complex compounds synthesized by sol–gel method. *Catal. Commun.*, **2007**, *8*(11), 1743-1747. https://doi.org/10.1016/j.catcom.2007.01.036

16. S.-H. Jo, B. Shin, M.-C. Shin, C.J. Van Tyne, and H. Lee. Dispersion and valence state of $MnO_2/Ce_{(1-x)}Zr_xO_2–TiO_2$ for low temperature NH_3–SCR. *Catal. Commun.*, **2014**, *57*, 134-137. https://doi.org/10.1016/j.catcom.2014.08.014

17. E. Y. Liberman, B. S. Kleusov, A. V. Naumkin, I. V. Zagaynov, T. V. Konkova, E. A. Simakina, and A. O. Izotova. Thermal stability and catalytic activity of the $MnO_x–CeO_2$ and the $MnO_x–ZrO_2–CeO_2$ highly dispersed materials in the carbon monoxide oxidation reaction. *Inorg. Mater. Appl. Res.*, **2021**, *12*(2), 468-476. https://doi.org/10.1134/s2075113321020325

18. T. N. Afonasenko, D. V. Glyzdova, V. L. Yurpalov, V. P. Konovalova, V. A. Rogov, E. Y. Gerasimov, and O. A. Bulavchenko. The study of thermal stability of Mn–Zr–Ce, Mn–Ce and Mn–Zr oxide catalysts for CO oxidation. *Materials*, **2022**, *15*(21), 7553. https://doi.org/10.3390/ma15217553

19. M. V. Grabchenko, G. V. Mamontov, M. V. Chernykh, O. V. Vodyankina, and M. A. Salaev. Synergistic effect in ternary CeO_2–ZrO_2–MnO_x catalysts for CO oxidation and soot combustion. *Chem. Eng. Sci.*, **2024**, *285*, 119593. https://doi.org/10.1016/j.ces.2023.119593

20. M. Wang, Y. Zhang, Y. Yu, W. Shan, and H. He. Surface oxygen species essential for the catalytic activity of Ce–M–Sn (M = Mn or Fe) in soot oxidation. *Catal. Sci. Technol.*, **2021**, *11*(3), 895-903. https://doi.org/10.1039/d0cy02077j

21. E. Y. Liberman, E. A. Simakina, I. A. Moiseev, A. O. Izotova, T. V. Kon'kova, and V. N. Grunsky. Synthesis and activity of nanodispersed SnO_2–CeO_2 catalyst in the oxidation reactions of carbon monoxide and methane. *Kinet. Catal.*, **2021**, *62*(1), 155-159. https://doi.org/10.1134/s0023158420060051

22. S. Zhu, S. Shi, X. Zheng, X. Wang, G. Yu, Y. Jiang, J. Feng, L. Zhu, and G. Zhang. Enhanced oxygen vacancies in Ce-doped SnO_2 nanofibers for highly efficient soot catalytic combustion. *Catalysts*, **2022**, *12*(6), 596. https://doi.org/10.3390/catal12060596

23. P.-O. Larsson and A. Andersson. Oxides of copper, ceria promoted copper, manganese and copper manganese on Al_2O_3 for the combustion of CO, ethyl acetate and ethanol. *Appl. Catal., B*, **2000**, *24*(3/4), 175-192. https://doi.org/10.1016/s0926-3373(99)00104-6

24. Y. Hasegawa, K. Fukumoto, T. Ishima, H. Yamamoto, M. Sano, and T. Miyake. Preparation of copper-containing mesoporous manganese oxides and their catalytic performance for CO oxidation. *Appl. Catal., B*, **2009**, *89*(3/4), 420-424. https://doi.org/10.1016/j.apcatb.2008.12.023

25. N. A. Sokovikov, D. A. Svintsitskiy, V. M. Metalnikova, S. V. Cherepanova, and A. I. Boronin. A $CuMnO_2$ based copper-manganese catalyst for low-temperature CO oxidation. *J. Struct. Chem.*, **2023**, *64*(6), 1098-1113. https://doi.org/10.1134/s0022476623060124

26. J. Li, P. Zhu, S. Zuo, Q. Huang, and R. Zhou. Influence of Mn doping on the performance of CuO–CeO_2 catalysts for selective oxidation of CO in hydrogen-rich streams. *Appl. Catal., A*, **2010**, *381*(1/2), 261-266. https://doi.org/10.1016/j.apcata.2010.04.020

27. M. Li, D.-H. Wang, X.-C. Shi, Z.-T. Zhang, and T.-X. Dong. Kinetics of catalytic oxidation of CO over copper-manganese oxide catalyst. *Sep. Purif. Technol.*, **2007**, *57*(1), 147-151. https://doi.org/10.1016/j.seppur.2007.03.016

28. A. A. Mirzaei, H. R. Shaterian, R. W. Joyner, M. Stockenhuber, S. H. Taylor, and G. J. Hutchings. Ambient temperature carbon monoxide oxidation using copper manganese oxide catalysts: Effect of residual Na^+ acting as catalyst poison. *Catal. Commun.*, **2003**, *4*(1), 17-20. https://doi.org/10.1016/s1566-7367(02)00231-5

29. X. Qiu, J. W. Thompson, and S. J. L. Billinge. PDFgetX2: a GUI-driven program to obtain the pair distribution function from X-ray powder diffraction data. *J. Appl. Crystallogr.*, **2004**, *37*(4), 678. https://doi.org/10.1107/s0021889804011744

30. C. L. Farrow, P. Juhas, J. W. Liu, D. Bryndin, E. S. Božin, J. Bloch, T. Proffen, and S. J. L. Billinge. PDFfit2 and PDFgui: computer programs for studying nanostructure in crystals. *J. Phys. Condens. Matter*, **2007**, *19*(33), 335219. https://doi.org/10.1088/0953-8984/19/33/335219

31. R. Evans. Density functionals in the theory of non-uniform fluids. In: Fundamentals of Inhomogeneous Fluids / Ed. D. Henderson. Mercel Dekker, **1992**, 85-175.

32. E. P. Barrett, L. G. Joyner, and P. P. Halenda. The determination of pore volume and area distributions in porous substances. I. Computations from nitrogen isotherms. *J. Am. Chem. Soc.*, **1951**, *73*(1), 373-380. https://doi.org/10.1021/ja01145a126

33. J. H. Scofield. Hartree-Slater subshell photoionization cross-sections at 1254 and 1487 eV. *J. Electron Spectrosc. Relat. Phenom.*, **1976**, *8*(2), 129-137. https://doi.org/10.1016/0368-2048(76)80015-1

34. D. A. Shirley. High-resolution X-ray photoemission spectrum of the valence bands of gold. *Phys. Rev. B*, **1972**, *5*(12), 4709-4714. https://doi.org/10.1103/physrevb.5.4709

35. R. D. Shannon. Revised effective ionic radii and systematic studies of interatomic distances in halides and chalcogenides. *Acta Crystallogr., Sect. A*, **1976**, *32*(5), 751-767. https://doi.org/10.1107/s0567739476001551

36. V. P. Pakharukova, D. I. Potemkin, V. N. Rogozhnikov, O. A. Stonkus, A. M. Gorlova, N. A. Nikitina, E. A. Suprun, A. S. Brayko, V. A. Rogov, and P. V. Snytnikov. Effect of Ce/Zr composition on structure and properties of $Ce_{1-x}Zr_xO_2$ oxides and related $Ni/Ce_{1-x}Zr_xO_2$ catalysts for CO_2 methanation. *Nanomaterials*, **2022**, *12*(18), 3207. https://doi.org/10.3390/nano12183207

37. S. A. Mock, S. E. Sharp, T. R. Stoner, M. J. Radetic, E. T. Zell, and R. Wang. CeO_2 nanorods-supported transition metal catalysts for CO oxidation. *J. Colloid Interface Sci.*, **2016**, *466*, 261-267. https://doi.org/10.1016/j.jcis.2015.12.026

38. M.-F. Luo, P. Fang, M. He, and Y.-L. Xie. In situ XRD, Raman, and TPR studies of CuO/Al_2O_3 catalysts for CO oxidation. *J. Mol. Catal. A: Chem.*, **2005**, *239*(1/2), 243-248. https://doi.org/10.1016/j.molcata.2005.06.029

39. G. Águila, F. Gracia, J. Cortés, and P. Araya. Effect of copper species and the presence of reaction products on the activity of methane oxidation on supported CuO catalysts. *Appl. Catal., B*, **2008**, *77*(3/4), 325-338. https://doi.org/10.1016/j.apcatb.2007.08.002

40. D. Fang, J. Xie, D. Mei, Y. Zhang, F. He, X. Liu, and Y. Li. Effect of $CuMn_2O_4$ spinel in Cu–Mn oxide catalysts on selective catalytic reduction of NO_x with NH_3 at low temperature. *RSC Adv.*, **2014**, *4*(49), 25540. https://doi.org/10.1039/c4ra02824d

41. T. N. Afonasenko, D. V. Yurpalova, Z. S. Vinokurov, A. A. Saraev, E. E. Aidakov, V. P. Konovalova, V. A. Rogov, and O. A. Bulavchenko. The formation of Mn–Ce–Zr oxide catalysts for CO and propane oxidation: The role of element content ratio. *Catalysts*, **2023**, *13*(1), 211. https://doi.org/10.3390/catal13010211

42. O. A. Bulavchenko, Z. S. Vinokurov, T. N. Afonasenko, P. G. Tsyrul′nikov, S. V. Tsybulya, A. A. Saraev, and V. V. Kaichev. Reduction of mixed Mn–Zr oxides: In situ XPS and XRD studies. *Dalton Trans.*, **2015**, *44*(35), 15499-15507. https://doi.org/10.1039/c5dt01440a

43. E. S. Ilton, J. E. Post, P. J. Heaney, F. T. Ling, and S. N. Kerisit. XPS determination of Mn oxidation states in Mn (hydr)oxides. *Appl. Surf. Sci.*, **2016**, *366*, 475-485. https://doi.org/10.1016/j.apsusc.2015.12.159

44. J. W. Murray, J. G. Dillard, R. Giovanoli, H. Moers, and W. Stumm. Oxidation of Mn(II): Initial mineralogy, oxidation state and ageing. *Geochim. Cosmochim. Acta*, **1985**, *49*(2), 463-470. https://doi.org/10.1016/0016-7037(85)90038-9

45. J. L. Junta and M. F. Hochella. Manganese(II) oxidation at mineral surfaces: A microscopic and spectroscopic study. *Geochim. Cosmochim. Acta*, **1994**, *58*(22), 4985-4999. https://doi.org/10.1016/0016-7037(94)90226-7

46. N. S. McIntyre and M. G. Cook. X-ray photoelectron studies on some oxides and hydroxides of cobalt, nickel, and copper. *Anal. Chem.*, **1975**, *47*(13), 2208-2213. https://doi.org/10.1021/ac60363a034

47. D. A. Svintsitskiy, A. P. Chupakhin, E. M. Slavinskaya, O. A. Stonkus, A. I. Stadnichenko, S. V. Koscheev, and A. I. Boronin. Study of cupric oxide nanopowders as efficient catalysts for low-temperature CO oxidation. *J. Mol. Catal., A: Chem.*, **2013**, *368/369*, 95-106. https://doi.org/10.1016/j.molcata.2012.11.015

48. D. A. Svintsitskiy, T. Y. Kardash, O. A. Stonkus, E. M. Slavinskaya, A. I. Stadnichenko, S. V. Koscheev, A. P. Chupakhin, and A. I. Boronin. In situ XRD, XPS, TEM, and TPR study of highly active in CO oxidation CuO nanopowders. *J. Phys. Chem. C*, **2013**, *117*(28), 14588-14599. https://doi.org/10.1021/jp403339r

49. A. Wollner, F. Lange, H. Schmelz, and H. Knozinger. Characterization of mixed copper-manganese oxides supported on titania catalysts for selective oxidation of ammonia. *Appl. Catal., A*, **1993**, *94*(2), 181-203. https://doi.org/10.1016/0926-860x(93)85007-c

50. D. Terribile, A. Trovarelli, C. de Leitenburg, A. Primavera, and G. Dolcetti. Catalytic combustion of hydrocarbons with Mn and Cu-doped ceria–zirconia solid solutions. *Catal. Today*, **1999**, *47*(1-4), 133-140. https://doi.org/10.1016/s0920-5861(98)00292-2

51. T. N. Afonasenko, D. V. Glyzdova, V. P. Konovalova, A. A. Saraev, E. E. Aydakov, and O. A. Bulavchenko. Effect of calcination temperature on the properties of Mn–Zr–Ce catalysts in the oxidation of carbon monoxide. *Kinet*. *Catal*., **2022**, *63*(4), 431-439. https://doi.org/10.1134/s0023158422040012

52. E. A. Derevyannikova, T. Y. Kardash, L. S. Kibis, E. M. Slavinskaya, V. A. Svetlichnyi, O. A. Stonkus, A. S. Ivanova, and A. I. Boronin. The structure and catalytic properties of Rh-doped CeO_2 catalysts. *Phys*. *Chem*. *Chem*. *Phys*., **2017**, *19*(47), 31883-31897. https://doi.org/10.1039/c7cp06573f